Wang, X., Khodaparast, H. H., Shaw, A. D., Friswell, M. I., & Zheng, G. (2018). Localisation of local nonlinearities in structural dynamics using spatially incomplete measured data. *Mechanical Systems and Signal Processing*, *99*, 364-383. https://doi.org/10.1016/j.ymssp.2017.06.021

# Localisation of local nonlinearities in structural dynamics using spatially incomplete measured data

Xing Wang[a, b], Hamed Haddad Khodaparast[c], Alexander D. Shaw[c], Michael I. Friswell[c], Gangtie Zheng[a]

[a] School of Aerospace Engineering, Tsinghua University, Beijing 100084, China

[b] Department of Mechanical Engineering, University of Bristol, Bristol BS8 1TR, United Kingdom

[c] College of Engineering, Swansea University, Swansea SA1 8EN, United Kingdom

## Abstract

This paper presents a procedure to localise nonlinear elements using spatially incomplete measured frequency response data from the structural vibration test. The method does not require measurements of all the responses associated with nonlinear elements and the information about the types of nonlinear elements. In this procedure, the Craig-Bampton reduction method is employed to reduce the dynamic equation onto the measured region and to project the nonlinear forces onto the measured degrees of freedom (DOFs), which are then called reduced nonlinear forces (RNFs). It is shown that the reduced nonlinear forces are the sum of the measured nonlinear forces and the projections of the unmeasured nonlinear forces through the transpose of linear constraint modes. Therefore, by analysing and comparing the magnitude of the reduced nonlinear forces obtained from experiments with the linear constraint modes, we can localise the nonlinear elements without directly measuring their responses. Numerical simulations of a discrete system with two nonlinearities and experimental data from a clamped beam with a nonlinear connection are used to validate the localisation procedure.

**Keywords:** nonlinear model updating, spatially incomplete measurement, localisation of nonlinear elements

## 1. Introduction

Nonlinearity exists in a wide range of engineering structures and plays a key role in complicated structural behaviours such as multi-value responses and input-dependent frequency response functions. In contrast to the well-established modal testing schemes [1] or updating procedures [2] for linear structures, there is no universal or standard approach to experimental test of nonlinear structures, despite considerable research efforts.

The localisation of nonlinear elements, which is the subject of this paper, is an important step in the identification framework of multiple-degree-of-freedom (MDOF) nonlinear structures [3-6]. It can be used to detect unexpected faults, such as nonlinear cracks or failures, or unexpected nonlinear boundary conditions that were originally assumed to be linear. Using the location of nonlinear elements to separate the underlying linear and nonlinear parts of a MDOF structure has already proved to be a useful and robust way to formulate a well-conditioned identification procedure, especially for practical engineering structures with many DOFs. The locations of nonlinear elements can also reveal clear physical insights into the system and provide the necessary information to add additional nonlinear elements when improving the Finite Element (FE) model. Finally, the localisation should confirm engineering experience of real structures and give confidence in the results, i.e. potential nonlinear locations should correspond to the existence of joints, bearings, contacts, nonlinear materials, etc.

Input-dependent frequency response functions, and the lack of conventional modal decoupling and modal superposition techniques, provide significant challenges and raise several questions about the localisation process of nonlinear elements. The first question is whether the types of the nonlinear elements should be known before the localisation begins. Early studies [7-9] assumed that the types of nonlinearity should be pre-known or pre-identified. Candidate nonlinear forces (with some unknown variables) were applied to each DOF of the structure and the unknown variables were identified from the measured nonlinear responses; the DOFs with non-zero variables determine the

locations of the nonlinear elements. Kerschen *et al.* [3] recommended the localisation process as a second step after the detection of the nonlinearities, and thus no priori information of the nonlinearities should be assumed. Recently, Ewins *et al.* [4] placed 'characterisation of nonlinearity' ahead of 'location of nonlinearity' in their 'modal +' testing procedure, which naturally uses the type of nonlinearity as a priori information during the localisation process. In practice, it seems unlikely that the type of nonlinearity would be known, but the location would be known. One possibility is to build a library of every possible type of nonlinearity and use a brute-force method to explore every combination; this is very time consuming and risks numerical instability for structures with many DOFs.

Another question is whether all of the responses associated with the nonlinear elements have to be measured during the localisation process, which is equivalent to limiting the possible locations of the nonlinear elements to within the measured region. By using force identification methods [10, 11], the DOFs associated with the nonlinear elements do not have to be measured. However, the measured frequency response function (FRF) matrix must be inverted to extract the nonlinear forces, and this inversion is sensitive to the measurement noise and modelling errors. For linear structures we can use the modal superposition techniques or the nonlinear perturbation of the linear receptance to avoid the inversion [12]; however, this is not possible for nonlinear structures since superposition is no longer valid. A compromise is to assume that all of the DOFs associated with the nonlinear elements are included in the measured region [13-15], as shown in Fig. 1(a). As such, the dynamic equation can be partitioned into the measured and unmeasured regions. Since no nonlinear forces are assumed in the unmeasured region, the unmeasured responses can be estimated by the expansion of the measured responses [13-15]. This restriction is a severe limitation for the localisation of nonlinear elements [3,16], since for practical applications the DOFs directly associated with the nonlinear element are unlikely to be fully measured when their locations are unknown.

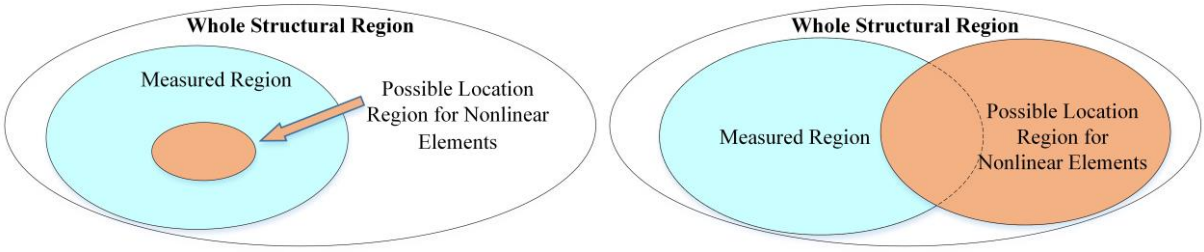


(a) (b)

**Fig. 1.** The region assumption of (a) the previous localisation procedure [13-15] and (b) the proposed localisation procedure.

The objective of this paper is to remove the restriction in the localisation procedure that requires full measurements of the DOFs associated with the nonlinearities, without using a priori information about the types of nonlinearities, as shown in Fig. 1(b). The localisation procedure starts with an initial linear FE model constructed for the underlying linear structure and updates it by the well-developed linear model updating technique [2] using data measured under a low amplitude excitation. Next, the reduced nonlinear forces are extracted by correlating the updated linear FE model to the data from the high amplitude stepped-sine excitation, and these forces are then compared with the linear constraint modes to determine the candidate DOFs included in the suspect region (possible location region for nonlinear elements), prior to finally localising the measured or unmeasured nonlinear elements and verifying the localisation results.

The rest of this paper is organised as follows. In Section 2, the proposed localisation procedure is introduced in detail. In Section 3, the localisation procedure is demonstrated and discussed using a twenty-DOF numerical example with two nonlinearities. An application of this procedure to localise a nonlinear mechanism of a clamped beam using experimental data is presented in Section 4. Conclusions are drawn in Section 5.

## 2. The localisation procedure

### 2.1. Formulation

Consider the general form of the dynamic equation of a MDOF discrete system with multiple nonlinearities as

$$\mathbf{M}\ddot{\boldsymbol{x}} + \mathbf{C}\dot{\boldsymbol{x}} + \mathbf{K}\boldsymbol{x} + \boldsymbol{f}^{*}\left(\boldsymbol{x}, \dot{\boldsymbol{x}}\right) = \boldsymbol{p}\left(t\right), \tag{1}$$

where $\mathbf{M}$ , $\mathbf{C}$ , $\mathbf{K}$ denote the mass, damping and stiffness matrices, respectively. $\boldsymbol{x}$ , $\dot{\boldsymbol{x}}$ , $\ddot{\boldsymbol{x}}$ denote the displacement, velocity and acceleration vectors, respectively. Vector $\boldsymbol{f}^{*}\left(\boldsymbol{x}, \dot{\boldsymbol{x}}\right)$ represents the nonlinear force and vector $\boldsymbol{p}\left(t\right)$ is the external excitation force.

To proceed, we define the measured and unmeasured regions, according to the placement of the sensors, as

$$\boldsymbol{x} = \begin{Bmatrix} \boldsymbol{x}_m \\ \boldsymbol{x}_u \end{Bmatrix}, \tag{2}$$

where the subscripts $\bullet_m$ and $\bullet_u$ denote the measured and unmeasured DOFs, respectively.

In this paper, we propose two types of test for a nonlinear structure: 1) low amplitude test, which often uses random excitations or low amplitude swept-sine inputs to produce homogeneous FRFs, which are independent of the input levels. The responses measured from this test are called the responses of the underlying linear structure and the FE model updated using this data is called the underlying linear model; 2) high amplitude test that typically uses high level stepped-sine or swept-sine excitations where nonlinear distortions in the responses are often observed. The input forces applied to the structure are also measured. Also, we consider moderate damping for the nonlinear structure, and the structural response is assumed to be dominated by the primary harmonic term under high amplitude testing [6,12,13-16].

Before the localisation procedure is developed using the data from these two types of tests, the following major assumptions are made:

1) The number of modes of the underlying linear structure, in the frequency range of interest, is less than the number of sensors (often less than half of the number of the sensors), and typically far less than the total number of DOFs in the structure.
2) During structural vibration tests, the sensors are well placed and are able to accurately capture, in the frequency range of interest, the modal frequencies and modal shapes of the underlying linear structure.
3) An initial linear FE model of the underlying linear structure is available and its modelling errors after updating are small. The measurement noise is also small.
4) The effects of nonlinearities in the system can be captured by the responses taken from high amplitude tests. The measured nonlinear responses, in the frequency range of interest, are sensitive to the adjustment of the nonlinear elements.
5) The number of independent nonlinear elements is less than the number of sensors.

The first two assumptions correspond to the basic requirements of sensor placement for a linear structural test and the third assumption shows that this procedure requires an updated linear model [2]. The fourth assumption ensures the structure is nonlinear and the measured responses contain enough information to localise the nonlinear elements. The final assumption then guarantees the robustness of the localisation procedure.

We now describe the details of the localisation procedure. The FRF data from a low amplitude excitation is used to update the underlying linear FE model using the well-established algorithms from the literature [2], which will not be introduced in detail here. This low amplitude data will also be used to compare with the high amplitude response data and perform the data selection of the high amplitude data, which is described in Section 2.2. Using the selected data, the reduced nonlinear forces (RNFs) are extracted with the updated linear FE model. Its main process and features will be

introduced in Section 2.3. Sections 2.4 and 2.5 describe the preliminary location decision process and its verification criteria, respectively. The proposed localisation procedure is summarised by a flow chart, shown in Fig. 2.

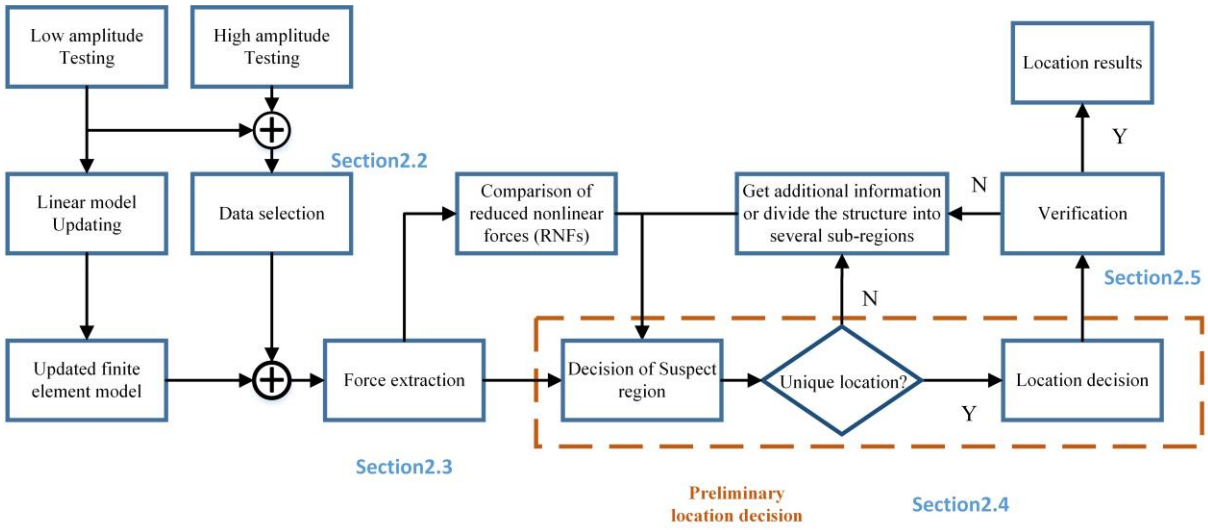


**Fig. 2.** Flow chart of the proposed localisation procedure.

### 2.2. Data selection

In order to improve the robustness of the localisation procedure, and to filter the measurement noise and modelling error, an important step is to select the data measured using the high amplitude input and to ensure that the selected frequency range of data is truly affected by the nonlinearities, as depicted in Fig. 2. Here, we first define the deviation of measured data, $\boldsymbol{\varepsilon}_m$, between responses using low amplitude and high amplitude inputs, as

$$\boldsymbol{\varepsilon}_m = \boldsymbol{X}_m^{\text{High}} - \mathbf{H}_{mm}^{\text{Low}} \boldsymbol{P}_m^{\text{High}}, \tag{3}$$

in which, $\mathbf{H}_{mm}^{\text{Low}}$ is the FRFs measured using a low amplitude excitation, $\boldsymbol{X}_m^{\text{High}}$ is the measured nonlinear response data using the high amplitude input, and $\boldsymbol{P}_m^{\text{High}}$ is its corresponding input force.

Then, we choose a constant threshold, $\Delta_s$, as the criteria to preserve only a selected frequency range of data for the subsequent force extraction. The selected frequencies need to satisfy

$$\left\| \boldsymbol{\varepsilon}_m(\omega_l) \right\|_\infty > \Delta_s, \tag{4}$$

where $\|\bullet\|_\infty$ denotes the infinity norm. Usually $\Delta_s \approx \left\|\boldsymbol{X}_m^{\text{High}}\right\| \times (2\% - 5\%)$ is sufficient to filter the measurement noise and modelling errors [16], where $\|\bullet\|$ denotes the Euclidean norm.

### 2.3. Force extraction

Having the selected data and the updated linear model using the mature theory [1,2], we now correlate these data to the updated linear model and extract the nonlinear forces (as shown in Fig. 2), instead of using the inversion of the transfer function matrix [10,11]. First, let us partition the dynamic equations of Eq. (1) into the measured and unmeasured regions, yielding

$$\begin{bmatrix} \mathbf{M}_{mm} & \mathbf{M}_{mu} \\ \mathbf{M}_{um} & \mathbf{M}_{uu} \end{bmatrix} \begin{Bmatrix} \ddot{\boldsymbol{x}}_m \\ \ddot{\boldsymbol{x}}_u \end{Bmatrix} + \begin{bmatrix} \mathbf{C}_{mm} & \mathbf{C}_{mu} \\ \mathbf{C}_{um} & \mathbf{C}_{uu} \end{bmatrix} \begin{Bmatrix} \dot{\boldsymbol{x}}_m \\ \dot{\boldsymbol{x}}_u \end{Bmatrix} + \begin{bmatrix} \mathbf{K}_{mm} & \mathbf{K}_{mu} \\ \mathbf{K}_{um} & \mathbf{K}_{uu} \end{bmatrix} \begin{Bmatrix} \boldsymbol{x}_m \\ \boldsymbol{x}_u \end{Bmatrix} + \begin{Bmatrix} \boldsymbol{f}_m^* \\ \boldsymbol{f}_u^* \end{Bmatrix} = \begin{Bmatrix} \boldsymbol{p}_m \\ \boldsymbol{p}_u \end{Bmatrix}, \tag{5}$$

where vectors $\boldsymbol{f}_m^*$ and $\boldsymbol{f}_u^*$ denote the nonlinear forces in the measured and unmeasured regions. Note that the nonlinear force vector in the unmeasured region, $\boldsymbol{f}_u^*$, is not zero, whilst vector $\boldsymbol{p}_u$ is zero as the input is measured for a controlled test.

The next step is to reduce the order of the nonlinear model defined by Eq. (5) with the Craig-Bampton reduction using the linear model. The reduction transformation is

$$\begin{Bmatrix} \boldsymbol{x}_m \\ \boldsymbol{x}_u \end{Bmatrix} = \begin{bmatrix} \mathbf{I}_{mm} & \mathbf{0} \\ \boldsymbol{\Psi}_{um} & \boldsymbol{\Phi}_{uk} \end{bmatrix} \begin{Bmatrix} \boldsymbol{x}_m \\ \boldsymbol{\eta}_k \end{Bmatrix}, \tag{6}$$

where $\boldsymbol{\Phi}_{uk}$ is the matrix of mass normalised, fixed interface modal shapes, $\boldsymbol{\Psi}_{um}$ denotes the matrix of constraint modes, $\mathbf{I}_{mm}$ is the identity matrix, and $\boldsymbol{\eta}_k$ denotes the fixed interface modal coordinates. According to the Craig-Bampton reduction method, the fixed interface modes can be obtained by solving the following generalised eigenvalue problem for the unmeasured region,

$$\left(\mathbf{K}_{uu} - \omega_i^2 \mathbf{M}_{uu}\right) \boldsymbol{\phi}_i = 0, \quad \text{with: } i = 1, 2, \cdots, k, \tag{7}$$

which gives the eigenvectors $\boldsymbol{\phi}_1, \boldsymbol{\phi}_2, \ldots \boldsymbol{\phi}_k$ and their corresponding eigenvalues, $\omega_1^2, \omega_2^2, \ldots \omega_k^2$. Therefore, the matrices of fixed interface modes and eigenvalues are

$$\boldsymbol{\Phi}_{uk} = \left[\boldsymbol{\phi}_1 \quad \boldsymbol{\phi}_2 \quad \cdots \quad \boldsymbol{\phi}_k\right], \tag{8}$$

$$\boldsymbol{\Lambda}_{kk} = \mathrm{diag}\left[\omega_1^2, \omega_2^2, \cdots, \omega_k^2\right]. \tag{9}$$

Note that the number of fixed interface modes, $k$, retained for further analysis should be sufficient to produce accurate underlying linear dynamics in the frequency range of interest.

In the Craig-Bampton reduction method, the matrix of constraint modes in Eq. (6) is obtained as

$$\boldsymbol{\Psi}_{um} = -\mathbf{K}_{uu}^{-1}\mathbf{K}_{um}. \tag{10}$$

Having all the matrices in the reduction transformation matrix in Eq. (6), the Craig-Bampton reduction is created by substituting Eq. (6) into Eq. (5), and pre-multiplying Eq. (5) by the transpose of the transformation matrix, which leads to

$$\begin{bmatrix} \overline{\mathbf{M}}_{mm} & \overline{\mathbf{M}}_{mk} \\ \overline{\mathbf{M}}_{km} & \mathbf{I}_{kk} \end{bmatrix} \begin{Bmatrix} \ddot{\boldsymbol{x}}_m \\ \ddot{\boldsymbol{\eta}}_k \end{Bmatrix} + \begin{bmatrix} \overline{\mathbf{C}}_{mm} & \overline{\mathbf{C}}_{mk} \\ \overline{\mathbf{C}}_{km} & \boldsymbol{\xi}_{kk} \end{bmatrix} \begin{Bmatrix} \dot{\boldsymbol{x}}_m \\ \dot{\boldsymbol{\eta}}_k \end{Bmatrix} + \begin{bmatrix} \overline{\mathbf{K}}_{mm} & \mathbf{0} \\ \mathbf{0} & \boldsymbol{\Lambda}_{kk} \end{bmatrix} \begin{Bmatrix} \boldsymbol{x}_m \\ \boldsymbol{\eta}_k \end{Bmatrix} + \begin{Bmatrix} \boldsymbol{\Psi}_{um}^{\mathrm{T}} \boldsymbol{f}_u^* + \boldsymbol{f}_m^* \\ \boldsymbol{\Phi}_{uk}^{\mathrm{T}} \boldsymbol{f}_u^* \end{Bmatrix} = \begin{Bmatrix} \boldsymbol{p}_m \\ \mathbf{0} \end{Bmatrix}, \tag{11}$$

where $\mathbf{I}_{kk}$ is the identity matrix and $\boldsymbol{\Lambda}_{kk}$ is defined by Eq. (9). The reduced mass, damping and stiffness matrices are

$$\begin{aligned}
&\overline{\mathbf{M}}_{mm} = \boldsymbol{\Psi}_{um}^{\mathrm{T}}\mathbf{M}_{uu}\boldsymbol{\Psi}_{um} + \mathbf{M}_{mu}\boldsymbol{\Psi}_{um} + \boldsymbol{\Psi}_{um}^{\mathrm{T}}\mathbf{M}_{um} + \mathbf{M}_{mm}, && \overline{\mathbf{M}}_{mk} = \boldsymbol{\Psi}_{um}^{\mathrm{T}}\mathbf{M}_{uu}\boldsymbol{\Phi}_{uk} + \mathbf{M}_{mu}\boldsymbol{\Phi}_{uk}, \\
&\overline{\mathbf{M}}_{km} = \boldsymbol{\Phi}_{uk}^{\mathrm{T}}\mathbf{M}_{uu}\boldsymbol{\Psi}_{um} + \boldsymbol{\Phi}_{uk}^{\mathrm{T}}\mathbf{M}_{um}, && \overline{\mathbf{C}}_{mm} = \boldsymbol{\Psi}_{um}^{\mathrm{T}}\mathbf{C}_{uu}\boldsymbol{\Psi}_{um} + \mathbf{C}_{mu}\boldsymbol{\Psi}_{um} + \boldsymbol{\Psi}_{um}^{\mathrm{T}}\mathbf{C}_{um} + \mathbf{C}_{mm}, \\
&\overline{\mathbf{C}}_{mk} = \boldsymbol{\Psi}_{um}^{\mathrm{T}}\mathbf{C}_{uu}\boldsymbol{\Phi}_{uk} + \mathbf{C}_{mu}\boldsymbol{\Phi}_{uk}, && \overline{\mathbf{C}}_{km} = \boldsymbol{\Phi}_{uk}^{\mathrm{T}}\mathbf{C}_{uu}\boldsymbol{\Psi}_{um} + \boldsymbol{\Phi}_{uk}^{\mathrm{T}}\mathbf{C}_{um}, \\
&\boldsymbol{\xi}_{kk} = \boldsymbol{\Phi}_{uk}^{\mathrm{T}}\mathbf{C}_{uu}\boldsymbol{\Phi}_{uk}, && \overline{\mathbf{K}}_{mm} = \mathbf{K}_{mm} + \mathbf{K}_{mu}\boldsymbol{\Psi}_{um},
\end{aligned} \tag{12}$$

In this paper, the high amplitude test of the structure uses a harmonic force input, $\boldsymbol{p}_m$, and the structure is assumed to have moderate damping, such that the steady-state response is dominated by the primary harmonic term [6,12,13-16]. Now we apply the Fourier transform to Eq. (11) and balance the primary harmonic terms, yielding

$$\begin{bmatrix} \overline{\mathbf{D}}_{mm} & \overline{\mathbf{D}}_{mk} \\ \overline{\mathbf{D}}_{km} & \overline{\mathbf{D}}_{kk} \end{bmatrix} \begin{Bmatrix} \boldsymbol{X}_m \\ \mathbf{N}_k \end{Bmatrix} + \begin{Bmatrix} \boldsymbol{\Psi}_{um}^{\mathrm{T}}\boldsymbol{F}_u^* + \boldsymbol{F}_m^* \\ \boldsymbol{\Phi}_{uk}^{\mathrm{T}}\boldsymbol{F}_u^* \end{Bmatrix} = \begin{Bmatrix} \boldsymbol{P}_m \\ \mathbf{0} \end{Bmatrix}, \tag{13}$$

in which $\boldsymbol{X}_m$, $\mathbf{N}_k$, $\boldsymbol{F}_u^*$, $\boldsymbol{F}_m^*$ and $\boldsymbol{P}_m$ denote the amplitude of the primary harmonic term of $\boldsymbol{x}_m$, $\boldsymbol{\eta}_k$, $\boldsymbol{f}_u^*$, $\boldsymbol{f}_m^*$ and $\boldsymbol{p}_m$, respectively. The dynamic stiffness matrices are given by $\overline{\mathbf{D}}_{mm} = -\omega^2\overline{\mathbf{M}}_{mm} + \mathrm{j}\omega\overline{\mathbf{C}}_{mm} + \overline{\mathbf{K}}_{mm}$, $\overline{\mathbf{D}}_{mk} = -\omega^2\overline{\mathbf{M}}_{mk} + \mathrm{j}\omega\overline{\mathbf{C}}_{mk}$, $\overline{\mathbf{D}}_{km} = -\omega^2\overline{\mathbf{M}}_{km} + \mathrm{j}\omega\overline{\mathbf{C}}_{km}$ and $\overline{\mathbf{D}}_{kk} = -\omega^2\mathbf{I}_{kk} + \mathrm{j}\omega\boldsymbol{\xi}_{kk} + \boldsymbol{\Lambda}_{kk}$. $\omega$ denotes the forcing frequency, and j is the imaginary unit.

Looking at Eq.(13), the top equation can be written as

$$\overline{\mathbf{D}}_{mm}\boldsymbol{X}_m+\overline{\mathbf{D}}_{mk}\mathbf{N}_k+\left(\boldsymbol{\Psi}_{um}^{\mathrm{T}}\boldsymbol{F}_u^*+\boldsymbol{F}_m^*\right)=\boldsymbol{P}_m. \tag{14}$$

Defining the reduced nonlinear force, $\boldsymbol{F}_{\text{reduced}}^*$, as

$$\boldsymbol{F}_{\text{reduced}}^*=\boldsymbol{\Psi}_{um}^{\mathrm{T}}\boldsymbol{F}_u^*+\boldsymbol{F}_m^*, \tag{15}$$

then we have

$$\boldsymbol{F}_{\text{reduced}}^*=\boldsymbol{P}_m-\overline{\mathbf{D}}_{mm}\boldsymbol{X}_m-\overline{\mathbf{D}}_{mk}\mathbf{N}_k. \tag{16}$$

From assumptions 1 and 2 in Section 2.1, sufficient sensors are chosen and are well placed to capture the underlying linear modes in the frequency range of interest. The responses of the fixed-interface modes, which are often observed at higher frequencies than the modes that affected by nonlinear elements, can thus be approximated by the expansion of measured responses, as

$$\mathbf{N}_k\approx-\overline{\mathbf{D}}_{kk}^{-1}\overline{\mathbf{D}}_{km}\boldsymbol{X}_m. \tag{17}$$

Therefore, from Eqs. (16) and (17), we approximately obtain the reduced nonlinear forces, as

$$\boldsymbol{F}_{\text{reduced}}^*\approx\boldsymbol{P}_m-\left(\overline{\mathbf{D}}_{mm}-\overline{\mathbf{D}}_{mk}\overline{\mathbf{D}}_{kk}^{-1}\overline{\mathbf{D}}_{km}\right)\boldsymbol{X}_m. \tag{18}$$

Note that the approximation shown in Eq. (18) is reasonably accurate in the low frequency range, where the responses are highly affected by the nonlinearities [5] but totally different from the previous assumptions in the literature [13-15] that require $\boldsymbol{f}_{\text{u}}^*=\mathbf{0}$. To justify this, the accuracy of the approximation will be demonstrated and verified with the following numerical and experimental examples. Recall that the responses in the low frequency range contain enough information about the nonlinear elements, as confirmed by assumption 4 in Section 2.1. Therefore, the reduced nonlinear forces, obtained using these responses by Eq. (18), can be used to localise the nonlinear elements without the requirement of fully measuring them. An index of the reduced nonlinear force is defined over a range of measured frequencies at each measured DOF to compare the amplitude, as

$$\boldsymbol{I}_{\boldsymbol{F}^*_{\text{reduced}}} = \sum_{\omega_i} \left| \boldsymbol{F}^*_{\text{reduced}}\left(\omega_i\right) \right|. \tag{19}$$

### 2.4. Preliminary location decision

According to the definition given by Eq. (15), the reduced nonlinear force is a direct sum of the measured nonlinear force and the projection of unmeasured nonlinear force. It is calculated from measured high amplitude data through Eq. (18), but to localise the nonlinear elements, we need to separate the measured and unmeasured nonlinear forces from the reduced nonlinear force. Some additional approaches have to be developed:

1) As shown in Eq. (15), the unmeasured nonlinear force, $\boldsymbol{F}_u^*$, propagates to the measured region through the projection, $\boldsymbol{\Psi}_{um}^{\mathrm{T}}$, but the relative phases of the projected forces will be preserved as either 0° or 180°, since $\boldsymbol{\Psi}_{um}^{\mathrm{T}}$ is a real-valued matrix. However, the phases of the independent nonlinear forces in the measured region, $\boldsymbol{F}_m^*$, do not have a similar property. As such, it can be used as a dominant feature to distinguish the measured force and the projection of the unmeasured nonlinear force.
2) A nonlinear element connecting two DOFs will introduce a pair of nonlinear forces with opposite signs (phase difference locked to 180°) and the same amplitude.
3) Information from the actual structure can be included to narrow the suspect region, for example, possible locations may be identified for clearances, bearings, or joints, or the total number of nonlinear elements may be specified.
4) If the reduced nonlinear forces are too complex to yield any valuable information, we can still use the brute-force method and consider every possible combination of the candidate DOFs. Thus the final location result can be decided by assuming the minimum number of DOFs that able to fit the reduced nonlinear forces.

Using these approaches, we can determine a range of candidate DOFs, named as suspect region in this paper. It can be denoted by

$$\boldsymbol{F}_u^* = \mathbf{B}_u \left\{ F_{u_1}^* \quad F_{u_2}^* \quad \cdots \quad F_{u_\tau}^* \right\}^{\mathrm{T}}, \tag{20}$$

$$\boldsymbol{F}_m^* = \mathbf{B}_m \left\{ F_{m_1}^* \quad F_{m_2}^* \quad \cdots \quad F_{m_\upsilon}^* \right\}^{\mathrm{T}}, \tag{21}$$

where $\tau$ and $\upsilon$ denote the number of unmeasured and measured nonlinear forces in the suspect region; $\mathbf{B}_u$ and $\mathbf{B}_m$ are their respective input matrices.

Substituting Eqs. (20) and (21) into Eq. (15), we obtain

$$\left[ \boldsymbol{\Psi}_{um}^{\mathrm{T}} \mathbf{B}_u \quad \mathbf{B}_m \right] \boldsymbol{F}_{\text{suspect}}^* = \boldsymbol{F}_{\text{reduced}}^*, \tag{22}$$

where $\boldsymbol{F}_{\text{suspect}}^*$ denotes the nonlinear force in the suspect region, which includes both unmeasured and measured nonlinear forces. As shown in the right side of Eqs. (20) and (21), it is given by

$$\boldsymbol{F}_{\text{suspect}}^* = \left\{ F_{u_1}^* \quad F_{u_2}^* \quad \cdots \quad F_{u_\tau}^* \quad F_{m_1}^* \quad F_{m_2}^* \quad \cdots \quad F_{m_\upsilon}^* \right\}^{\mathrm{T}}. \tag{23}$$

The error vector $\boldsymbol{J}_{\text{err}}$ is defined as the residual of Eq. (22) resulting from separating the nonlinear forces from the reduced nonlinear forces. It can be written as

$$\boldsymbol{J}_{\text{err}} = \left[ \boldsymbol{\Psi}_{um}^{\mathrm{T}} \mathbf{B}_u \quad \mathbf{B}_m \right] \boldsymbol{F}_{\text{suspect}}^* - \boldsymbol{F}_{\text{reduced}}^*. \tag{24}$$

The nonlinear force in the suspect region, $\boldsymbol{F}_{\text{suspect}}^*$, can thus be estimated by minimising the residual $\boldsymbol{J}_{\text{err}}$, i.e.

$$\boldsymbol{F}_{\text{suspect}}^* = \underset{\boldsymbol{F}_{\text{suspect}}^*}{\text{ArgMin}} \left\| \boldsymbol{J}_{\text{err}} \right\|. \tag{25}$$

Since $\boldsymbol{F}_{\text{reduced}}^*$ can be obtained using the measured responses from the high amplitude test by Eq. (18), the sufficient and necessary condition to estimate the nonlinear force in the suspect region, $\boldsymbol{F}_{\text{suspect}}^*$, by Eq. (22) is

$$\text{rank}\left[ \boldsymbol{\Psi}_{um}^{\mathrm{T}} \mathbf{B}_u \quad \mathbf{B}_m \right] \geq \tau + \upsilon. \tag{26}$$

From assumption 5 in Section 2.1, there are fewer independent nonlinear elements than the number of sensors. Therefore, Eq. (26) would be easily satisfied. If Eq. (26) is not satisfied because an excessive number of coordinates are suspected, we can divide the suspect region into several sub-regions that satisfying Eq. (26) and check each sub-region at a time. For these situations, multiple localisation scenarios may be obtained and need to be investigated further by

looking at the number of nonlinear DOFs or referring to additional information about the structure before the final decision of localisation result.

Likewise, we can also define the index of nonlinear forces at each candidate DOF in the suspect region, as

$$\boldsymbol{I}_{\boldsymbol{F}^*_{\text{suspect}}} = \sum_{\omega_i} \left| \boldsymbol{F}^*_{\text{suspect}}\left(\omega_i\right) \right| \tag{27}$$

The amplitudes and the phases of the nonlinear force can be further analysed and compared. For example, the inter-connected nonlinear elements can be further identified where the two forces have the same amplitudes but with a constant phase difference of 180°.

### 2.5. Verification

For a correct localisation of all the nonlinear elements, the equation error of Eq. (24) should be small and should satisfy

$$\left\| \boldsymbol{J}_{\text{err}} \right\| << \left\| \boldsymbol{F}^*_{\text{reduced}} \right\|. \tag{28}$$

If the above criterion is not met, then the localisation results are incorrect or the suspect region is inadequate. As such, the suspect region should be redefined or divided into serval sub-regions and the localisation procedure restarted, as summarised in Fig. 2. The localisation results are finally determined after meeting the verification criterion.

## 3. Numerical example

We now demonstrate the application of the localisation procedure to a twenty-DOF numerical example with two discrete nonlinear elements. As illustrated in Fig. 3, the system has a cubic stiffness spring connecting DOFs 6 and 17, and a grounded piecewise linear spring located at DOF 12. The system is excited at DOF 1 with a 20N stepped-sine force from 5Hz to 46Hz with a frequency resolution of 0.25 Hz in the high amplitude test; this frequency range covers the first six linear modes of the system, as summarised in Table 1. The spatially incomplete measurement is simulated

by assuming that only ten DOFs (odd numbered DOFs) are measured. As such, the responses of DOFs 6 and 12 are not measured but they are actual locations of the nonlinear elements.

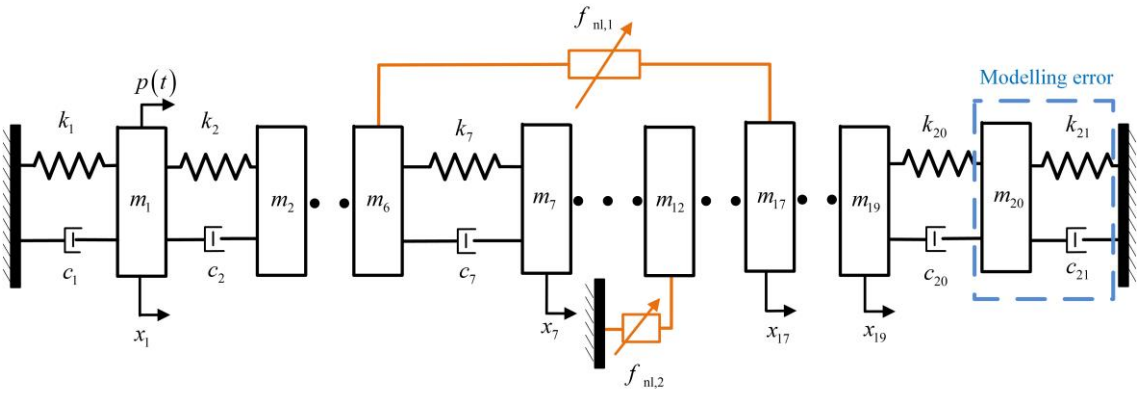


**Fig. 3.** A twenty-DOF system with two discrete nonlinear elements.

The physical parameters considered for this system are $m_1 = m_2 = \cdots = m_{20} = 1\text{kg}$, $k_1 = k_2 = \cdots = k_{21} = 1\times10^5$ N/ m, and the proportional damping is assumed as

$$\mathbf{C} = \alpha\mathbf{M} + \beta\mathbf{K}, \text{ with: } \alpha=2 \text{ and } \beta=5\times10^{-4}. \tag{29}$$

Table 1 gives the first six natural frequencies and modal damping ratios of the underlying linear system.

**Table 1**

The first six modal properties of the underlying linear system

| Mode number | Modal frequency (Hz) | Modal damping ratio (%) |
|---|---|---|
| 1 | 7.5222 | 3.2974 |
| 2 | 15.0024 | 3.4174 |
| 3 | 22.3986 | 4.2289 |
| 4 | 29.6696 | 5.1969 |
| 5 | 36.7747 | 6.2093 |
| 6 | 43.6741 | 7.2247 |

The cubic stiffness spring (between DOFs 6 and 17) of the system is given as

$$f_{\text{nl},1} = k^*_{\text{nl},1}\left(x_{17} - x_6\right)^3, \text{ with: } k^*_{\text{nl},1}=1\times10^{12}\ \text{N/m}^3, \tag{30}$$

and the model of piecewise linear spring (grounded at DOF 12) is denoted by

$$f_{\mathrm{nl},2}=\begin{cases}0 & x_{12}\le d\\ k^{*}_{\mathrm{nl},2}\left(x_{12}-d\right) & x_{12}>d\end{cases},\ \text{with: } d=1\times10^{-4}\,\mathrm{m}\ \text{and}\ k^{*}_{\mathrm{nl},2}=1\times10^{5}\ \mathrm{N/m}. \tag{31}$$

Direct time integration was used to obtain the responses of the system via a 4th order Runge-Kutta procedure in MATLAB. For each stepped-sine input scenario, a total of 500 cycles were computed with a time step that divides each excitation cycle into 1000 equal steps. The Fourier coefficients of the steady-state response and the input force at the excitation frequency were obtained by transforming the data of the last 250 cycles into the frequency domain. The first 250 cycles were discarded since they were computed just to ensure the transients have decayed.

### 3.1. Localisation results with no modelling error and noise free data

The localisation procedure was first performed with an accurate analytical model of the underlying linear system and noise free stepped-sine response data. Fig. 4 shows the indices of reduced nonlinear forces in the measured region obtained by Eq. (18), where reduced nonlinear forces at DOFs 5, 7, 11, 13 and 17 are significantly higher than those at the other measured DOFs.

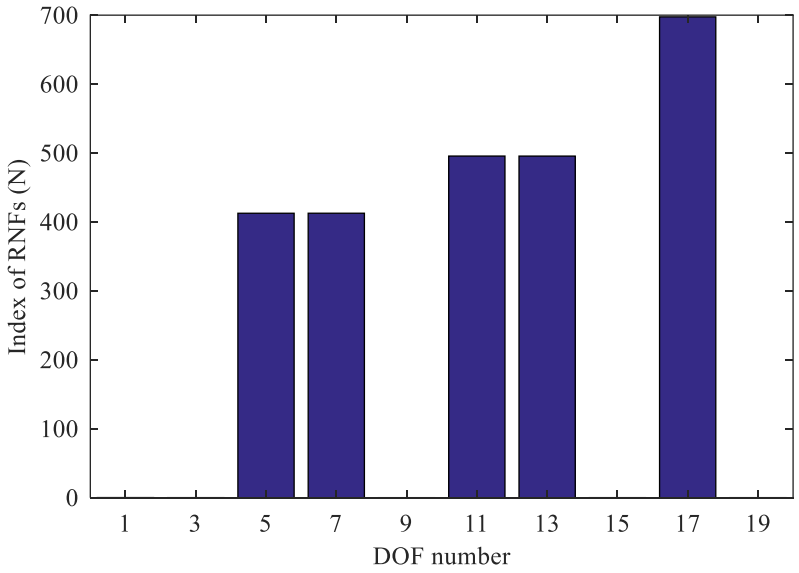


**Fig. 4.** The indices of the reduced nonlinear force in the measured region.

The high reduced nonlinear forces at DOFs 5, 7, 11, 13 and 17 indicate potential nonlinear elements near these DOFs. To gain more insights, Fig. 5 depicts the magnitudes and phases of the reduced nonlinear force at DOF 5 and DOF 7. It can be seen that their phases are exactly the same, which indicates that these two reduced nonlinear forces are derived from a single unmeasured nonlinear force, according to the discussions in Section 2.4. A similar conclusion can be drawn by comparing the reduced nonlinear forces between DOFs 11 and 13, as shown in Fig. 6. Note that the magnitudes of the reduced nonlinear forces at DOFs 11 and 13, in the frequency range from 32.25Hz to 37.75Hz shown in Fig. 6(a), are too small to obtain the phases, thus they are discarded in Fig. 6(b).

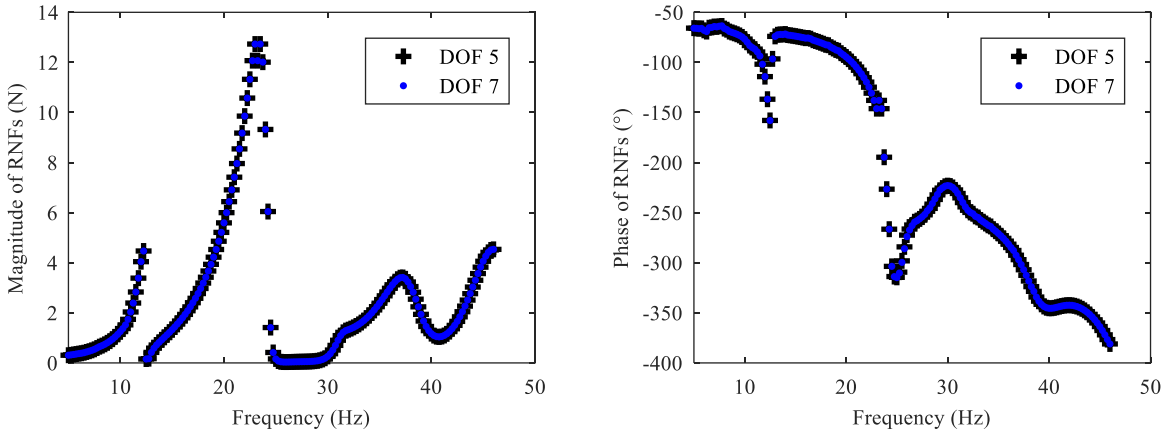


(a) (b)

**Fig. 5.** Comparison of the reduced nonlinear forces at DOFs 5 and 7. The two plots show (a) magnitude and (b) phase.

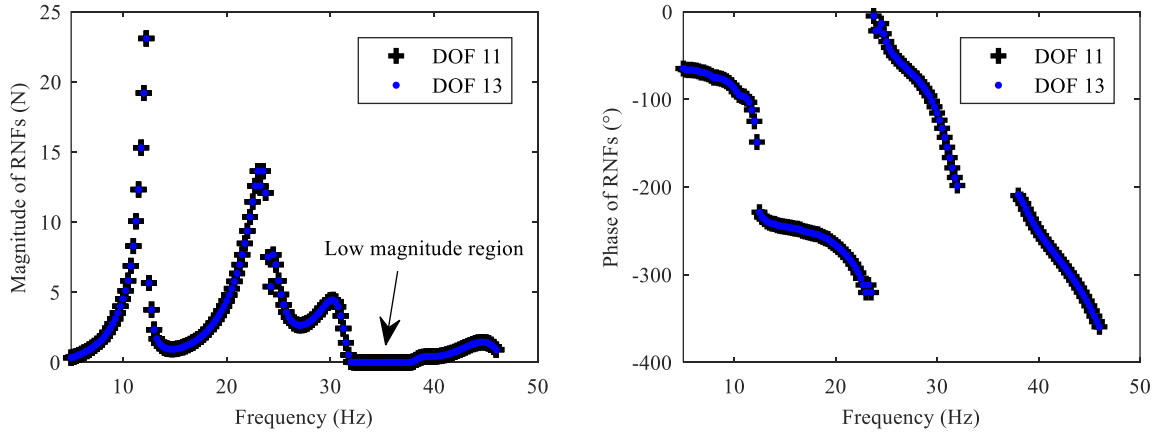

(a) (b)

**Fig. 6.** Comparison of the reduced nonlinear forces at DOFs 11 and 13. The two plots show (a) magnitude and (b) phase.

From the underlying linear model, the matrix of constraint modes, $\boldsymbol{\Psi}_{um}$, is

$$\boldsymbol{\Psi}_{um}=\begin{bmatrix} 0.5 & 0.5 & & \cdots & 0 \\ & 0.5 & 0.5 & & \vdots \\ \vdots & & \ddots & \ddots & \\ & & & 0.5 & 0.5 \\ 0 & & \cdots & & 0.4545 \end{bmatrix} \tag{32}$$

From the analysis in Section 2.4, the unmeasured nonlinear forces can only project onto the measured region through the transpose of constraint modes, $\boldsymbol{\Psi}_{um}^{\mathrm{T}}$, as expressed by Eq. (32). It is seen from Eq. (32) that only a nonlinear force at DOF 6 will project equally to both DOFs 5 and 7, and only a nonlinear force at DOF 12 will cause a pair of reduced nonlinear forces at DOFs 11 and 13 with the same amplitudes. Therefore, the measured DOFs 5, 7, 11 and 13 were removed from the suspect region and the unmeasured DOFs 6 and 12 were considered, as shown in Fig. 7.

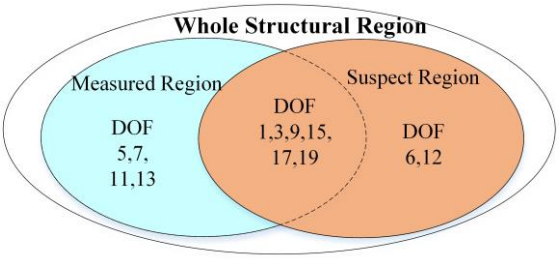


**Fig. 7.** The suspect region for the localisation of nonlinear elements.

Using Eq. (25), the nonlinear forces in the suspect region were extracted, as shown by the accumulated indices in Fig. 8. The nonlinear forces at DOFs 6, 12 and 17 are several orders higher than those at other DOFs; thus the location of nonlinear elements can be preliminary decided at DOFs 6, 12 and 17. It is verified by

$$\left\|\boldsymbol{J}_{\mathrm{err}}\right\| \approx 2.27\times10^{-4}\times\left\|\boldsymbol{F}^{*}_{\mathrm{reduced}}\right\|. \tag{33}$$

which indicates a small residual when estimating the nonlinear forces using Eq. (25).

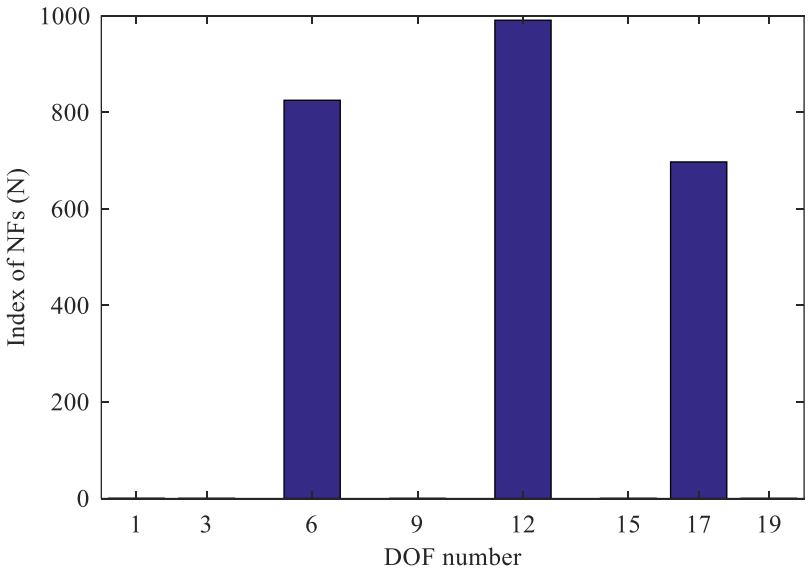


**Fig. 8.** The indices of nonlinear force in the suspect region.

Furthermore, Fig. 9 compares the nonlinear forces at DOFs 6 and 17, which clearly shows that they have the same amplitudes in the low frequency range but their phase differences are locked to 180°. This indicates that a nonlinear element is connected between DOFs 6 and 17.

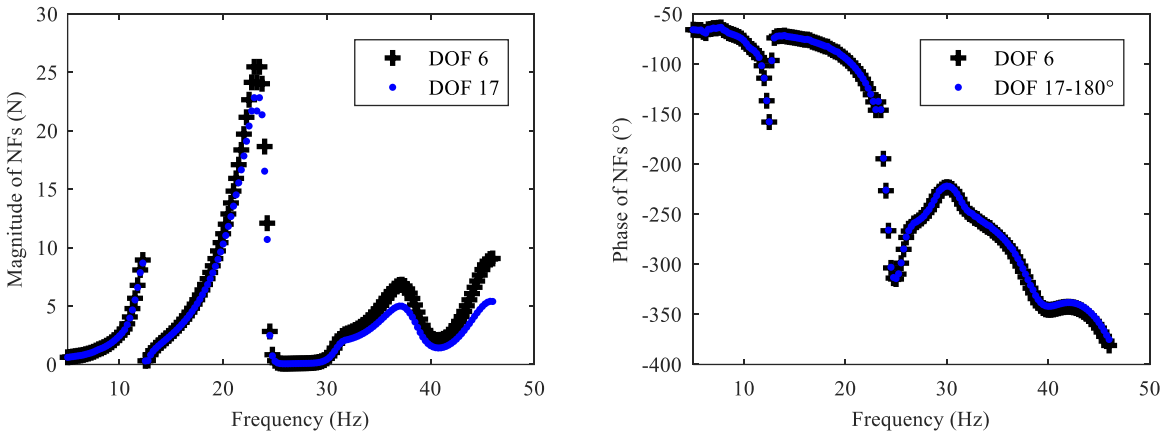


(a) (b)

**Fig. 9.** Comparison of the nonlinear forces at DOFs 6 and 17. The two plots show (a) magnitude and (b) phase.

Therefore, the final localisation result can be summarised as follows: one nonlinear element connecting DOFs 6 and 17; and one nonlinear element grounded at DOF 12. These conclusions correspond to the actual locations of the nonlinear elements.

### 3.2. Discussions

Here, the accuracy of the force approximation, Eq. (18), due to the spatially incomplete measurement is discussed first. Other effects, such as the modelling errors, the measurement noise and the structural damping levels, that are important to develop a robust localisation procedure will also be investigated.

#### 3.2.1. Accuracy of the force approximation

The nonlinear forces, used as an index to localise the nonlinear elements, are separated from the reduced nonlinear forces, and the reduced nonlinear forces are calculated by approximations due to spatially incomplete measurement, as shown by Eq. (18). The accuracy of this approximation in estimating the nonlinear forces, especially the unmeasured ones, is investigated for the numerical example by comparing the approximated forces to those obtained with full measurement [13]. Fig. 10 compares the nonlinear forces extracted at DOFs 6 and 12, where the cross points denote the approximated forces using ten measured responses (DOFs 6 and 12 are unmeasured) and the dotted points denote the actual nonlinear forces obtained with full measurement. It is seen that the approximation gives good estimates of the unmeasured nonlinear forces in the low frequency range.

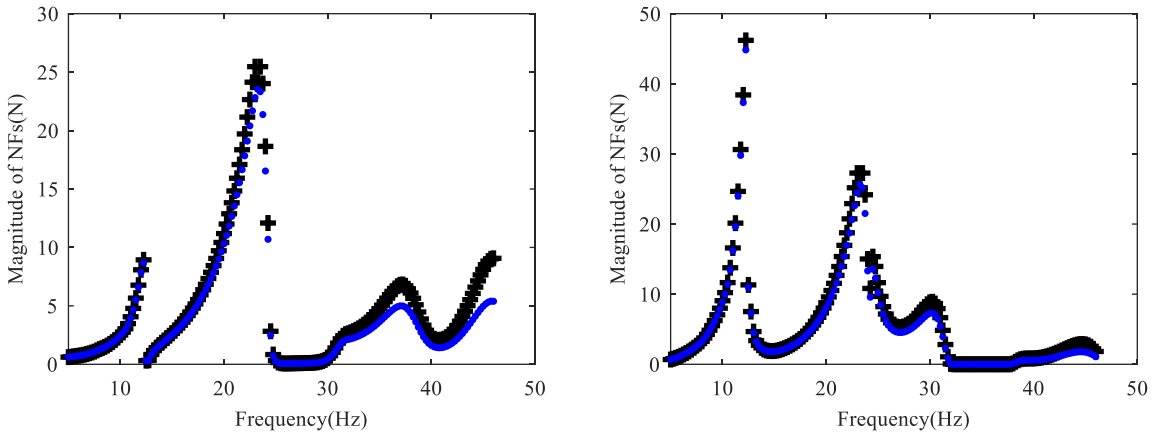


(a) (b)

**Fig. 10.** Comparison of the magnitudes of nonlinear force, where (✚) denotes the forces using spatially incomplete data with only odd numbered DOFs are measured and (•) denotes the forces using full measurement data. The two plots show nonlinear forces at (a) DOF 6 and (b) DOF 12.

We do observe deviations at high frequencies, such as the nonlinear force above 40 Hz at DOF 6, which indicates that we should only use data from the low frequency range for the localisation procedure. This justifies our fourth assumption in Section 2.1, which confirms that the response data in the low frequency range contains enough information to localise the nonlinear elements.

In the following discussions, only odd numbered DOFs are assumed to be measured.

### 3.2.2. Effect of the modelling error

The localisation procedure uses a FE model, which inevitably includes modelling errors. In order to simulate their effects, the linear stiffness denoted by $k_{21}$ in Fig. 3 is increased by different percentages. Fig. 11 depicts the underlying linear FRFs at DOFs 1 and 19, considering a modelling error of 20% in $k_{21}$.

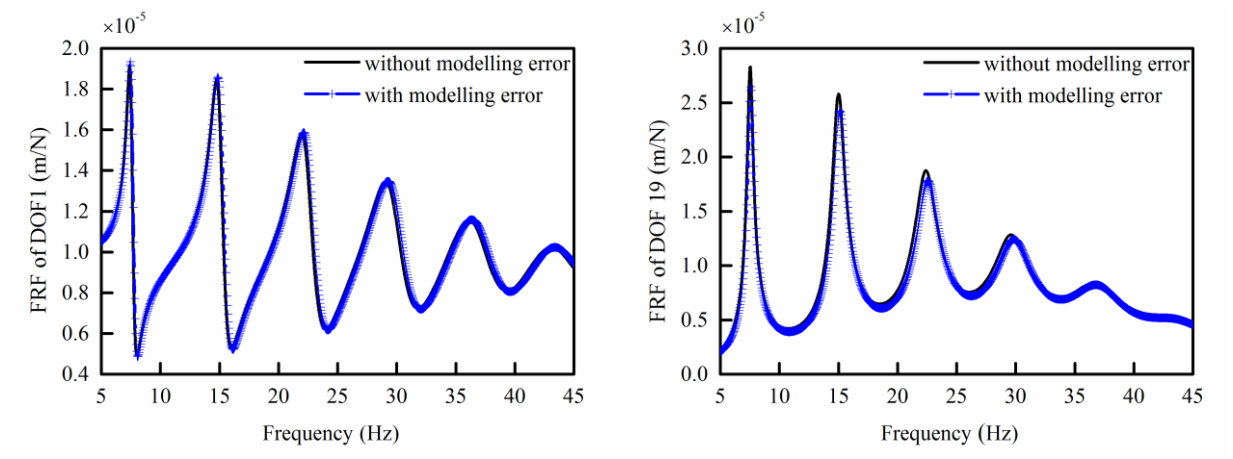


(a) (b)

**Fig. 11.** Comparison of underlying linear FRFs with/without 20% increase in $k_{21}$ at (a) DOF 1 and (b) DOF 19.

Firstly, the data selection was not employed and the effect of modelling error was studied. The modelling error was represented by increasing the value of $k_{21}$ by 5%, 10% and 20%, respectively. The localisation results in Fig. 12 show that the discrete modelling error introduces nonlinear forces at measured DOF 19, since its real location, DOF 20, was not measured. The index of this nonlinear force also increases with the level of modelling error. Nevertheless, it is always an order less than those DOFs associated with nonlinear elements for the maximum modelling error level we considered here (20%).

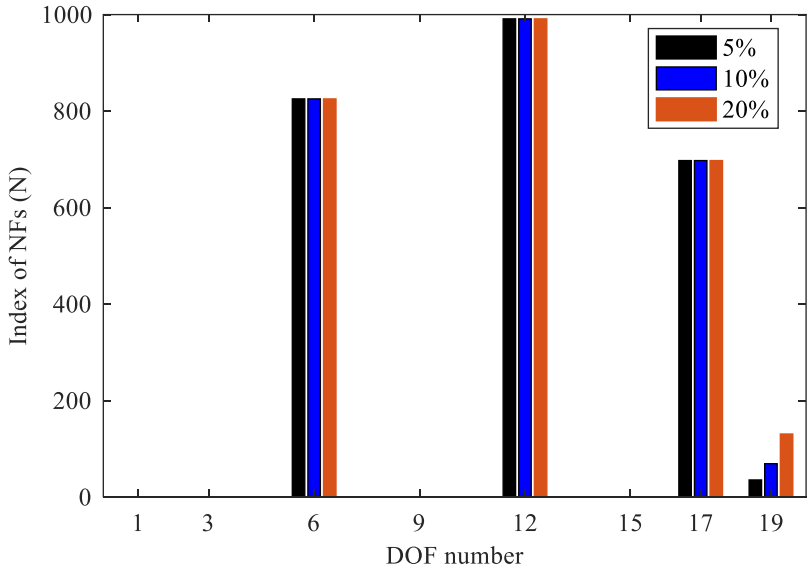

**Fig. 12.** The indices of nonlinear forces in the suspect region under different levels of modelling error in $k_{21}$.

Secondly, the error in $k_{21}$ was fixed at 20%, and the effect of data selection was investigated for three different threshold values, $\Delta_s$ =5e-5m, 1e-4m and 2e-4m. The results shown in Fig. 13 indicate that the nonlinear force corresponding to the modelling error can be suppressed by increasing the threshold value but the indices of actural nonlinear forces also decrease, since fewer measured points are selected. It is worth noting that the indices at DOF 19 are an order less than those at nonlinear DOFs, thus a good localisation result can be achieved.

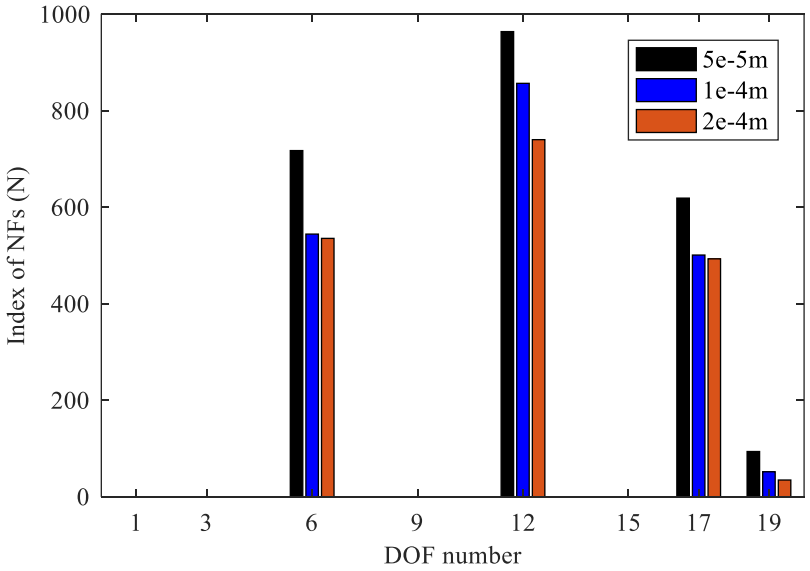


**Fig. 13.** The indices of nonlinear force in the suspect region for different values of the threshold.

### 3.2.3. Effect of the measurement noise

Another inevitable factor during experimental tests is the measurement noise, which causes two kinds of error in the localisation procedure: 1) the measurement noise in the low amplitude test introduces modelling errors in the underlying linear model; 2) the measurement noise in the high amplitude test results in errors in the estimated reduced nonlinear forces and nonlinear forces. Since the modelling error in underlying linear model has already been discussed in Section 3.2.2, here we just focus on the effects of measurement noise in the responses of the high amplitude test.

Consider the random noise matrix, $\mathbf{V}_{\text{noise}}$, as a set of independent and normally distributed vectors with zero mean and a standard deviation of $P_{\text{noise}}$ for the data in the high amplitude stepped-sine test. The responses are polluted by [16]

$$\boldsymbol{x}_m(\omega) = \boldsymbol{x}_m^{\text{nomial}}(\omega) + \mathbf{V}_{\text{noise}} \times \max\left[\text{abs}\left(\boldsymbol{x}_m^{\text{nomial}}(\omega)\right)\right]. \tag{34}$$

Firstly, the data selection was not employed and the effects of different noise levels were compared. Fig. 14 shows the indices of nonlinear force when the standard deviation of measurement noise, $P_{\text{noise}}$, was set to 0.5%, 1% and 2%. As seen that the indices in the linear region gradually increase with the noise level. However, even when the standard deviation reaches 2%, the indices at the linear DOFs are still far less than those at nonlinear DOFs, such that the locations of the nonlinear elements can be correctly identified at 2% noise level or below. It can be noted that in the high amplitude test, typically in the form of stepped-sine or swept-sine input, the system is excited at a single frequency such that the noise level in these tests would normally be less than 2%.

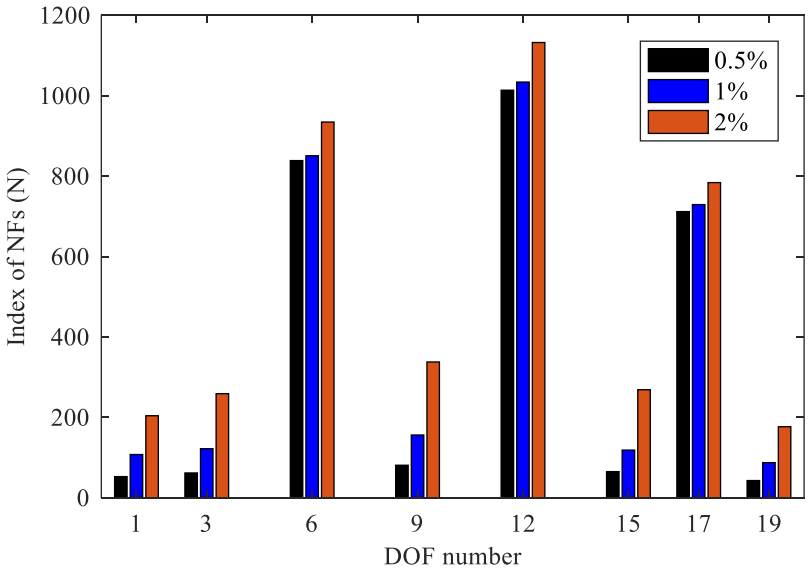


**Fig. 14.** The indices of nonlinear forces in the suspect region for different levels of the measurement noise.

Next, the measurement noise was kept at $P_{\text{noise}} = 2\%$, and the effect of the data selection was investigated for threshold, $\Delta_s$, chosen as 5e-5m, 2e-5m, and 2e-4 m. The results shown in Fig. 15 reveal that the data selection reduces

the estimated nonlinear forces at every suspect DOF, but the indices at DOFs associated with the nonlinear elements are always much higher compared to those in the linear region.

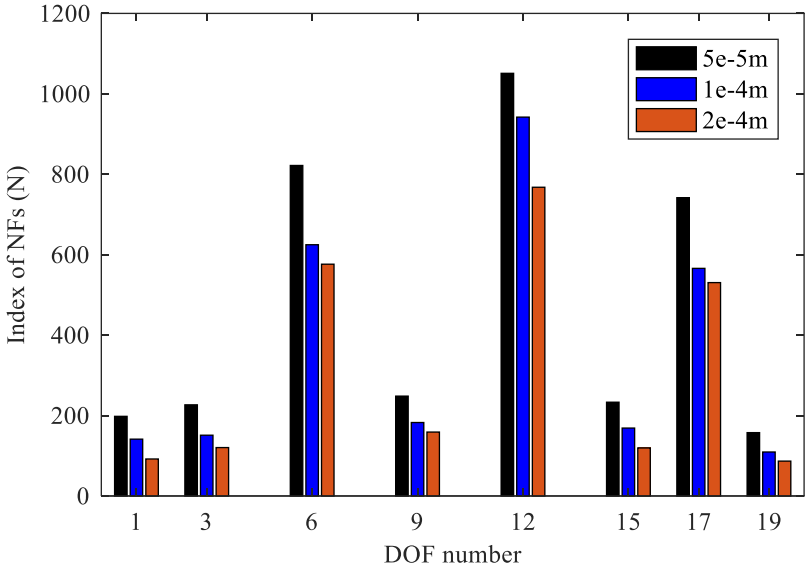


**Fig. 15.** The indices of nonlinear forces in the suspect region for different values of the threshold.

### 3.3.4. Effect of the system damping level

The damping level of the system also plays an important role in the localisation procedure. Here, we consider the system with 20% of the modelling error in $k_{21}$, 2% random error in the measurement and a threshold of $\Delta_s$ =2e-4m. The performance of proposed localisation procedure is examined for the system with different damping levels. To this end, the system damping level was reduced to 80% ( $\alpha$=1.6 , $\beta$=4×10$^{-4}$ and denoted as damping level 1), 50% ( $\alpha$=1 , $\beta$=2.5×10$^{-4}$ and denoted as damping level 2) and 30% ( $\alpha$=0.6 , $\beta$=1.5×10$^{-4}$ and denoted as damping level 3) of its original level defined by Eq. (29), whilst other parameters were not changed. The results are shown in Fig. 16. It can be seen that the indices of nonlinear forces increase with the decrease of system damping level. This is because the responses are larger and the system tends to be more nonlinear with less damping. Again, the indices of nonlinear forces

at DOFs 6, 12 and 17 are higher than the linear DOFs for each damping level considered here, thus a good localisation result can still be achieved.

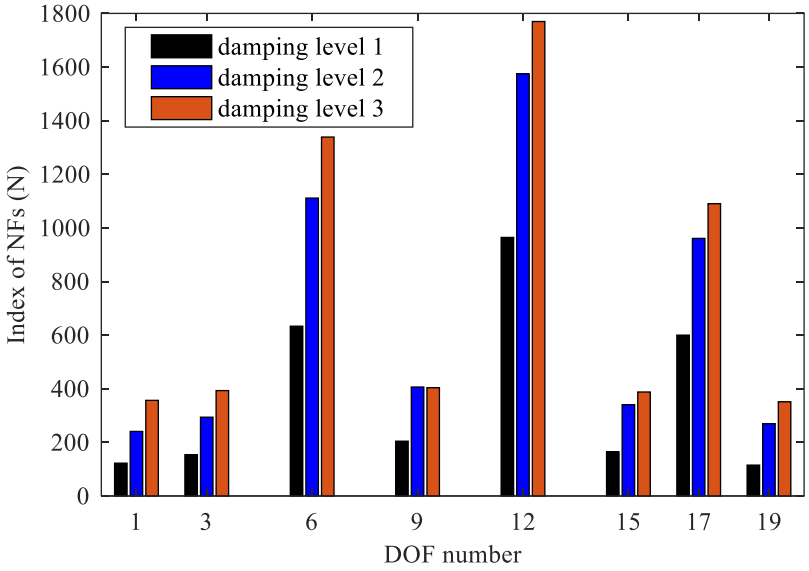


**Fig. 16.** The indices of nonlinear forces in the suspect region for the system with different damping levels. Damping levels 1, 2 and 3 correspond to 80%, 50% and 30% of the original damping level defined by Eq. (29).

## 4. Experimental example

In contrast to numerical systems with accurate underlying linear models containing simulated noise and errors, real life MDOF nonlinear structures face significant challenges during testing. For example, the nonlinear responses are more complicated, the noise may have non-zero mean, the idealisation modelling error cannot be identified, the rotational DOFs generally cannot be measured, and there are coupling effects between higher order harmonic responses and the shaker. In this section, an experimental study of the localisation procedure is presented based on a clamped beam with a nonlinear spring mechanism.

### 4.1. Experimental setup

Figure 17 shows a cantilever beam of length $0.38\text{m}$ with a nonlinear spring mechanism near the free end (at the location denoted by $a_2$). The motion of the beam is measured by five accelerometers (PCB 352 C03 piezoelectric accelerometers) at axial distances from the free end of 1cm ($a_1$), 10cm ($a_2$), 17.5cm ($a_3$), 23.5cm ($a_4$) and 34cm ($a_5$). The shaker is placed at 34cm from the free end.

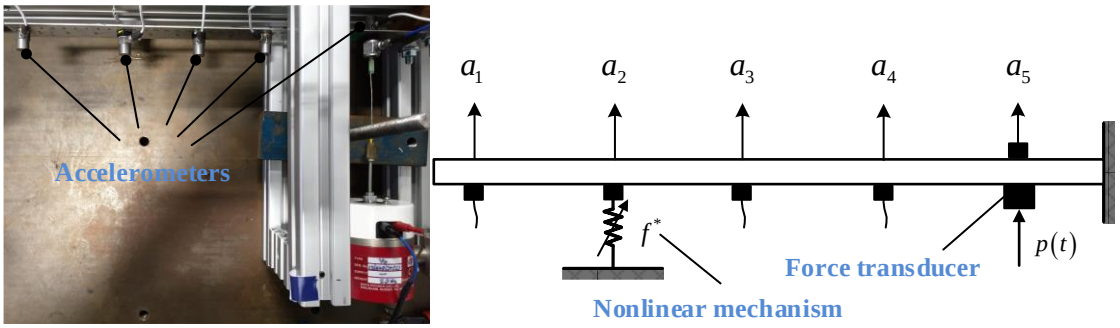


**Fig. 17.** The clamped beam with five distributed accelerometers.

The nonlinear mechanism consists of two linear springs arranged orthogonal to the movement of the connecting point, detailed in Fig. 18. Due to the unique geometrical relation of the two springs, the stiffness of this mechanism increases with the response and resulting in hardening effects [17]. In order to simulate a structure with an inaccessible nonlinear element, where the nonlinear mechanism exists in the unmeasured region, the measured data of the nonlinear mechanism ($a_2$) was not used during the location process. However, the responses of the mechanism were still recorded, together with the response at the other four DOFs (at locations $a_1$, $a_3$, $a_4$ and $a_5$) to validate the results obtained with the proposed procedure by comparing with the mature localisation methods that require a direct measurement at the nonlinear mechanism.

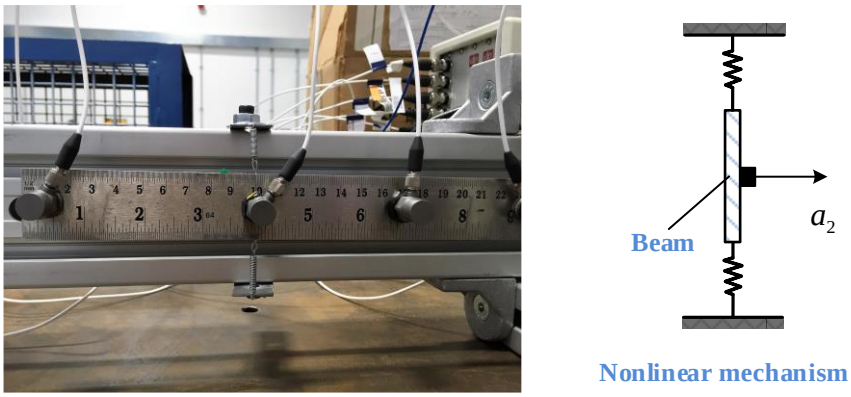


**Fig. 18.** The nonlinear spring mechanism.

### 4.2. Random testing and linear model updating

According to the procedure given in Fig. 2, the low amplitude random test of the beam was first performed with a Data Physics measurement system. The root mean square (RMS) force input was chosen as 0.5N and 1N, with a wide frequency bandwidth covering the first three linear modes of the beam. Figure 19 compares typical measured FRFs and the corresponding coherence functions at the beam tip ( $a_1$ ) for both forcing levels, indicating linear characters of the beam during these levels of testing.

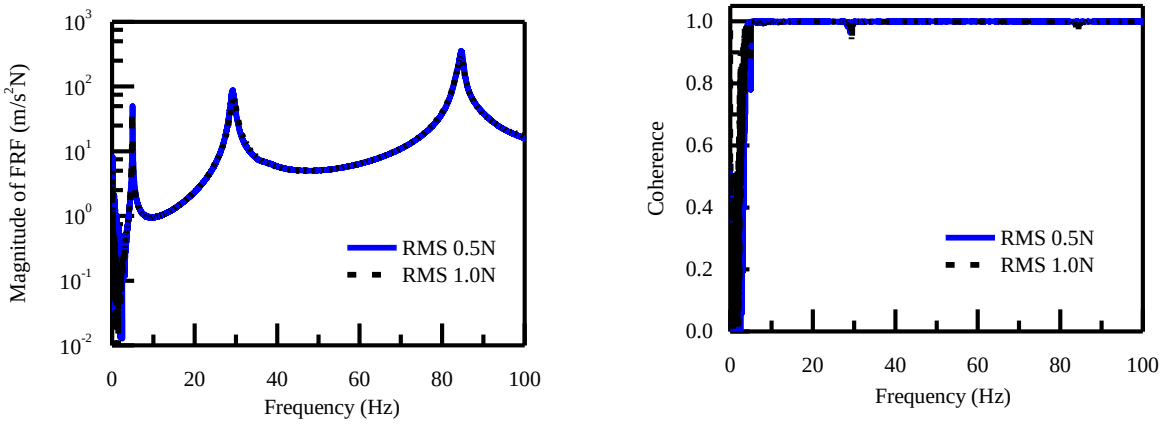


(a) (b)

**Fig. 19.** Linear acceleration FRFs measured at $a_1$ for two different forcing levels. The two plots show (a) magnitude and (b) coherence.

An FE model of the beam was created in MATLAB, in which the beam was discretised into 15 elements, since a refined model with 76 elements only shows a slight improvement (less than 0.004% differences for the modal frequencies). The accelerometers are modelled as 12g lumped masses and the force transducer is considered as a 30g lumped mass. The elastic modulus is chosen as 210 GPa , the beam width is 30 mm and the density is 7850 kg/m$^3$. As shown in Fig. 20, the flexibility at the root of the beam is considered and modelled by translational and rotational springs, with their stiffness coefficients to be updated. The thickness, the damping coefficients of the beam, the rotational stiffness of the stinger were also chosen to be updated in the linear updating process, as summarised in Table 2.

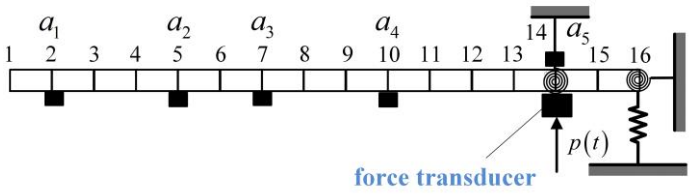


**Fig. 20.** An FE model of the 'clamped' beam.

The standard linear model updating procedure [2] was performed for the beam using the four FRFs obtained with 1N random excitation. It should be noted that the effective thickness of the beam was increased by 10.78% to account for the adhesive tape used as viscous damping layer to enhance the beam's damping. The proportional damping coefficients of the beam are determined by the first and third modes extracted from the measured data.

**Table 2**

Comparison of parameters before and after linear model updating

| Name | Original value | Updated value |
|---|---|---|
| Boundary translational stiffness | fixed | 394.01 kN/m |
| Boundary rotational stiffness | fixed | 258.38 Nm/rad |
| Beam thickness | 1 mm | 1.1078 mm |
| Rotational stiffness of stinger | 0.4858 Nm/rad | 0.0748 Nm/rad |
| Damping of the beam | 0.6% modal damping | proportional damping $\alpha=2.53e-1, \beta=2.15e-5$ |

### 4.3. Stepped-sine test and force extraction

High amplitude stepped-sine input was then applied on the structure. The coupling of the nonlinear response, which contains high order harmonics, with the stiffness and mass of the shaker, was alleviated by an active control strategy to produce high quality sinusoidal force inputs. The input voltage for the shaker amplifier was obtained by solving

$$\boldsymbol{P}(\boldsymbol{V}) - \tilde{\boldsymbol{P}} = \boldsymbol{0}, \tag{35}$$

where $\tilde{\boldsymbol{P}}$ denotes the desired harmonic force coefficients, and $\boldsymbol{P}(\boldsymbol{V})$ denotes the harmonic coefficients of the measured signal that actually excites the beam. When deviations are observed, feed forward control is activated based on the solution of Eq. (35); interested readers can refer to References [17] and [19] for more details. The control algorithm was programmed in LabVIEW real time programming module, and a cRIO-9024 embedded real-time controller was employed as the control hardware. Force and acceleration signals were recorded by NI9234 dynamic signal acquisition modules, and an NI9263 analog output module was used to generate the signals for the exciter.

During the experiment, the fifth harmonic of the structure was not evident, and thus only the primary and third harmonic terms were chosen as control parameters. The primary harmonic term of the input was set to the required level and the third harmonic coefficient of the input was controlled to zero. The maximum relative magnitude error in solving Eq. (35) was set to 1%, and the settling tolerance was also chosen as 1% by evaluating the harmonic coefficients of the responses at $a_1$ (near to the tip).

The stepped-sine test in this example was performed with active control. The force level was controlled at 1N with a frequency step of 0.025Hz during the sweep. It was observed that the higher modes of the beam were less affected by the nonlinear mechanism, and thus responses within the frequency range from 10Hz to 13Hz, as shown in Fig. 21, are utilised to localise the nonlinear element. Note that the lowest fixed interface modal frequency of the updated linear FE model (with four sensors) is 111.487Hz, which is significantly higher than the frequency range of the measured data.

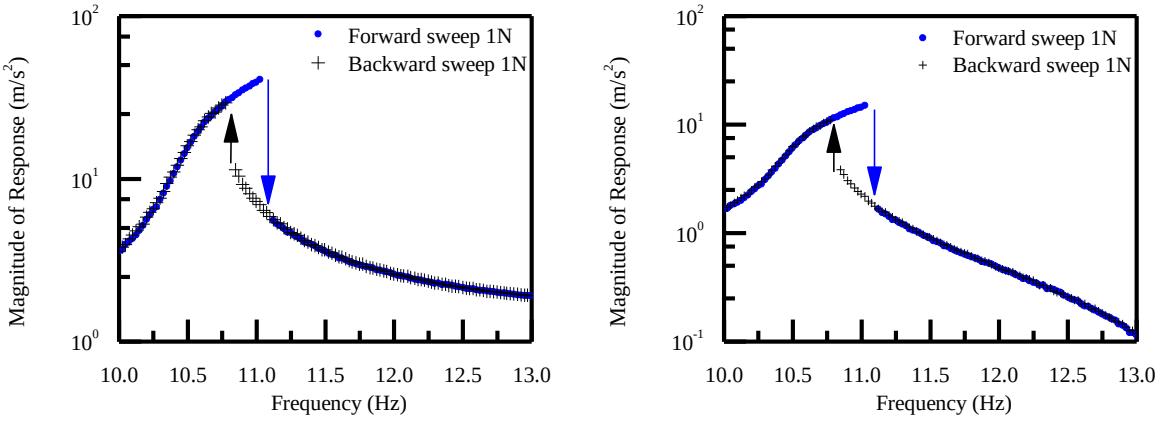


(a) (b)

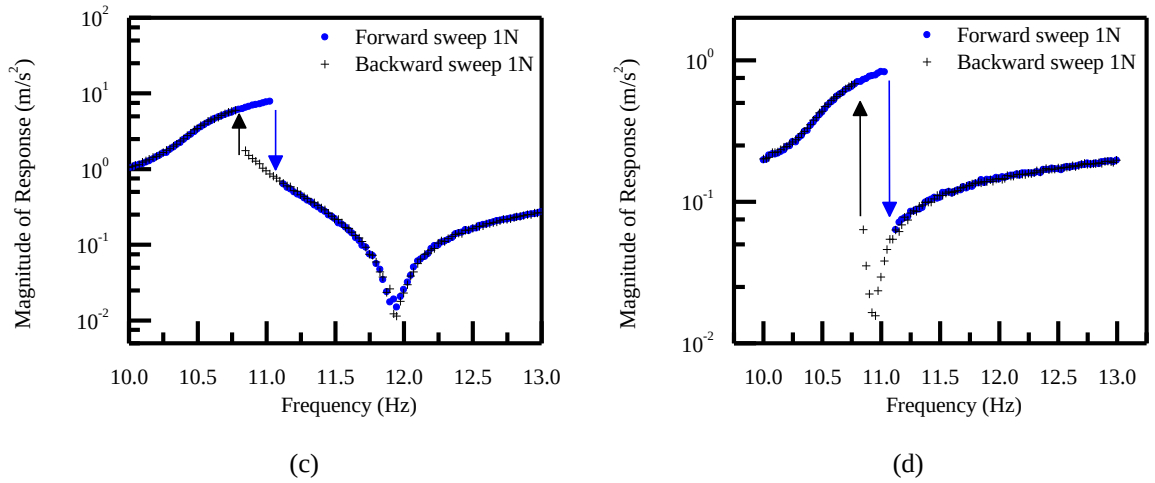


**Fig. 21.** The nonlinear responses for the forward and backward sweeps at (a) $a_1$, (b) $a_3$, (c) $a_4$ and (d) $a_5$.

Jumps occur during both forward and backward sweeps, with evidence of hardening effects. Since the forward sweep has higher response amplitudes, and hence a large effect due to the nonlinear mechanism, the localisation procedure will use this data (forward sweep responses). In the data selection stage, we choose a threshold of $\Delta_s = 5\,\mathrm{m/s^2}$ and the response data from 10.1Hz to 11.025Hz are selected by Eq. (4).

Fig. 22 shows the magnitudes and phases of the reduced nonlinear force in the measured region extracted from the measured data. As can be seen that the reduced nonlinear forces at $a_5$ are small and significantly affected by the noise; thus its phase is not plotted in Fig. 22 (b). Also note that the phases of the reduced nonlinear forces at $a_4$ has a constant difference of 180° with respect to the reduced nonlinear forces at $a_1$ and $a_3$, which indicates a potential nonlinear force in the unmeasured region. Fig. 23 compares the indices of reduced nonlinear forces in the measured region; the high values at $a_1$, $a_3$, and $a_4$ indicating that no direct information about the location of nonlinear elements can be found based on this plot.

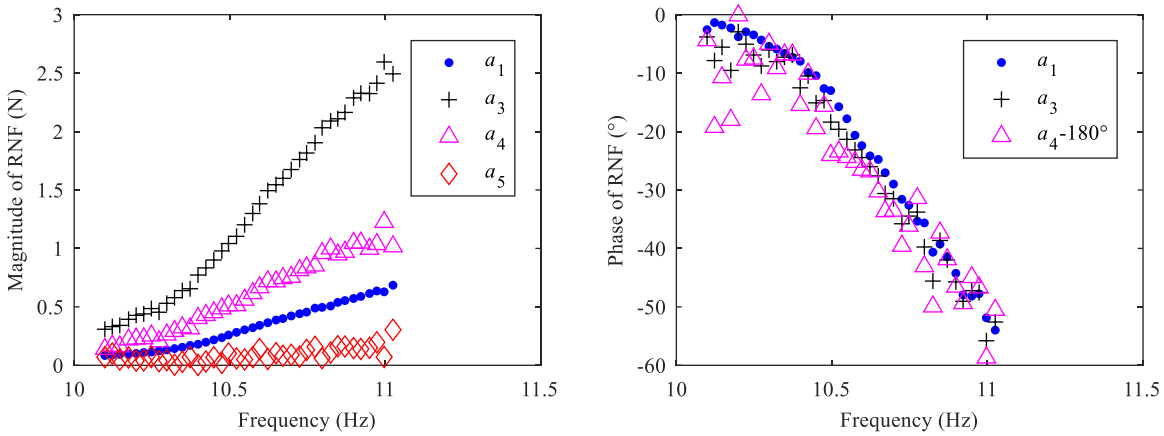


**Fig. 22.** The reduced nonlinear forces in the measured region. The two plots show (a) magnitude and (b) phase.

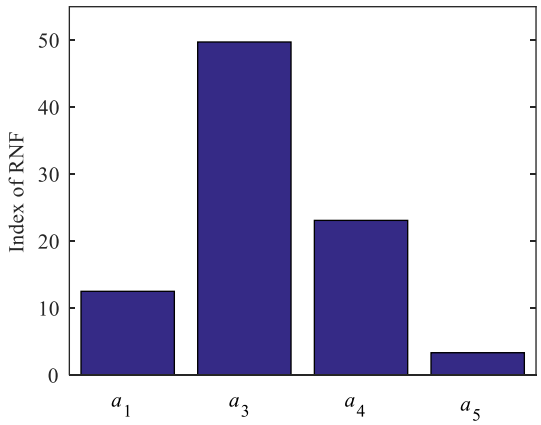


**Fig. 23.** The indices of reduced nonlinear force in the measured region.

### 4.4. Preliminary location decision

Section 2.4 highlighted that if the relative phases of the RNFs in measured region are always 0° or 180°, they are actually projections of the same unmeasured nonlinear force. In this experiment, as shown in Fig. 22, the good agreement among the phases of RNFs at DOF 3 ( $a_1$ ) and DOF 13 ( $a_3$ ), and a constant difference of 180° to DOF 19 ( $a_4$ ) indicates that they are the projections of one unmeasured force.

The analytical derivation of Eq. (15) reveals that the unmeasured nonlinear forces will project onto the measured region through the transpose of constraint modes, $\boldsymbol{\Psi}_{um}^{\mathrm{T}}$, which introduces the reduced nonlinear forces. Thus by comparing the ratio of the RNFs obtained from the experimental data with the ratios for the constraint modes calculated

from the updated FE model, we can find the location of the unmeasured nonlinear element. Note that the reduced nonlinear forces at $a_4$ have the opposite sign compared to the reduced nonlinear forces at $a_1$ and $a_3$. Thus, the unmeasured nonlinear force can only possibly exist between $a_1$ and $a_3$ according to the characteristic of the constraint modes of the beam. Fig. 24 compares the ratios of the reduced nonlinear force obtained from the experimental data with the ratios for the constraint modes for the unmeasured translational DOFs between $a_1$ and $a_3$. It is shown that the constraint mode at DOF 9 has good agreement with the experimental data, and thus DOF 9 is included in the suspect region, while DOF 3 ($a_1$), DOF 13 ($a_3$), and DOF 19 ($a_4$) are not suspected, i.e. only DOFs 9 and 27 are included in the suspect region. Fig. 25 compares the index of the nonlinear forces extracted from the experimental data, and the nonlinear force at the unmeasured DOF 9 is evidently high compared to that at DOF 27. Thus the location of nonlinear element can be preliminary decided to be at DOF 9.

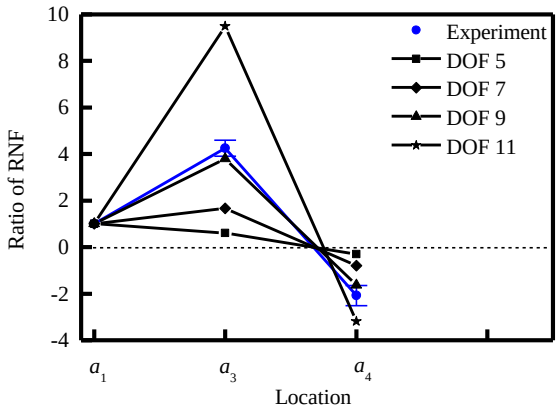


**Fig. 24.** The ratios of the reduced nonlinear force obtained from experiments and the constraint modes calculated from the updated linear FE model.

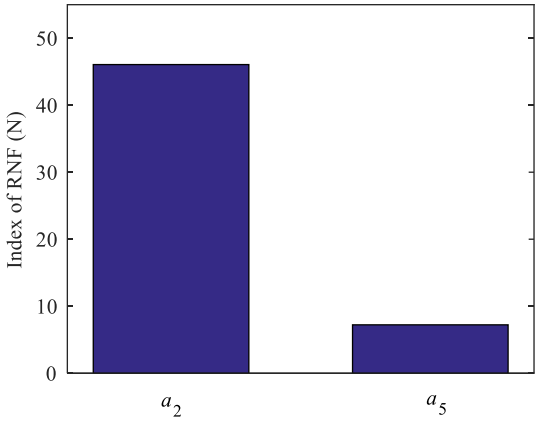


**Fig. 25.** The indices of nonlinear force in the suspect region.

### 4.4. Verification of the location results

The verification process is performed by checking Eq. (24), which shows the residuals of Eq. (25) obtained during the estimation of the nonlinear forces. In this experiment, we have

$$\left\|\boldsymbol{J}_{\text{err}}\right\| \approx 5\times10^{-2}\times\left\|\boldsymbol{F}^{*}_{\text{reduced}}\right\| \tag{36}$$

which verifies the preliminary location results and shows that the reduced nonlinear forces at DOF 3 ( $a_1$ ), DOF 13 ( $a_3$ ), and DOF 19 ( $a_4$ ) are projections of the nonlinear force at the unmeasured DOF 9 ( $a_2$ ). Thus, we can conclude that the nonlinear element exists at DOF 9, which is its real location as shown in Fig. 17 and Fig. 18.

The nonlinear force at DOF 9 can also be obtained with the well-established methods [13-15], which require the direct measurement of the DOF associated with the nonlinear element (DOF 9 at $a_2$ for this beam example) and assumes that the nonlinear elements only exist in the measured region. The magnitude of the FRF data at $a_2$ recorded during the experiment is shown in Fig. 26. Fig. 27 shows the indices of the nonlinear forces in the measured region using responses from five DOFs (including DOF 9), in which the nonlinear forces at DOF 9 are clear, also indicating the real location of the nonlinear element.

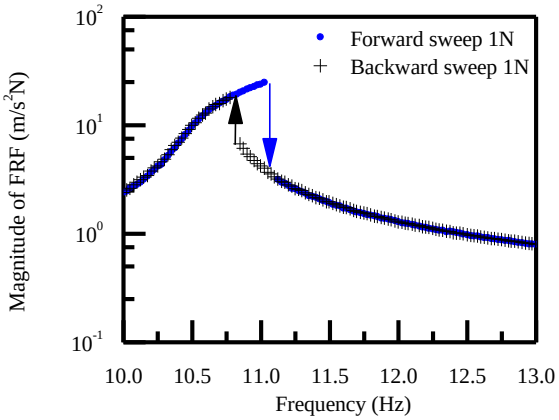


**Fig. 26.** The FRF for the forward and backward sweeps at $x_2$ .

The nonlinear forces obtained when DOF 9 ( $a_2$ ) is measured (using the methods in Refs [13-15]) and unmeasured (using the procedure proposed in this paper) are compared in Fig. 28; good agreement is achieved, which also validates the accuracy of nonlinear force extracted using the proposed method.

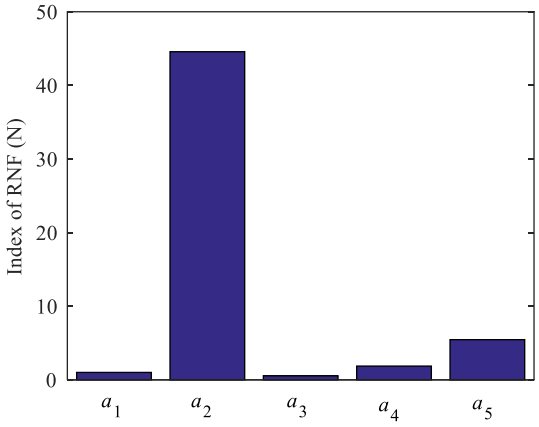


**Fig. 27.** The indices of nonlinear force in measured region with direct measurement at DOF 9 ( $a_2$ ).

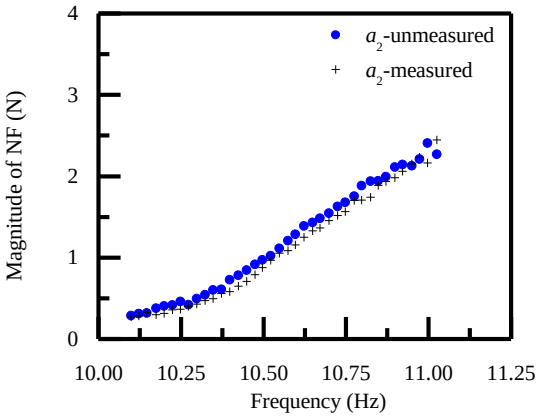

**Fig. 28.** The magnitudes of nonlinear force at DOF 9 with/without directly measuring the response at DOF 9 ( $a_2$ ).

## 5. Conclusions

This paper presents a procedure for the localisation of nonlinear elements using a spatially incomplete set of measured data from the structural vibrations test. In this procedure, the Craig-Bampton reduction method is employed to reduce the dynamic equation onto the measured region and to project the nonlinear forces onto the measured DOFs. It is shown that these reduced nonlinear forces are the sum of measured nonlinear forces and the projections of the unmeasured nonlinear forces by the transpose of constraint modes. By analysing and comparing the phases and magnitudes of the reduced nonlinear force obtained from experiments, we can obtain more information of the nonlinear elements and use this information to localise the forces. The localisation procedure uses a FE model of the underlying linear structure to avoid inversion of the measured FRF matrix, and thus increases the robustness of the procedure.

A twenty-DOF lumped mass system (only odd numbered DOFs are measured) was used to verify the localisation procedure, and to demonstrate the effects of simulated modelling error, measurement noise and system damping levels. This procedure was also applied to experimental data from a clamped beam with a nonlinear mechanism to validate its ability to localise nonlinear elements using experimental data.

The current nonlinear localisation procedure needs an initial FE model and a linear model updating process, which may be challenging for very complex structures with many DOFs. Also, the nonlinear response is assumed to be dominated by its primary harmonic term, which requires moderate damping in the structure.

**Acknowledgement**

The authors acknowledge the support of the National Natural Science Foundation of China (Grant No. 11272172). X.W. is also supported by the Engineering Nonlinearity programme grant EP/K003836/1. H.H.K acknowledge the support from EPSRC, grant number EP/P01271X/1.

**References**

[1] Ewins D J. Modal testing: theory and practice. Letchworth: Research studies press, 1995.

[2] Friswell M I, Mottershead J E. Finite element model updating in structural dynamics. Springer Science & Business Media, 1995.

[3] Kerschen G, Worden K, Vakakis A F, Golinval, J.-C. Past, present and future of nonlinear system identification in structural dynamics. Mechanical systems and signal processing, 2006, 20(3): 505-592.

[4] Ewins D J, Weekes B, delli Carri A. Modal testing for model validation of structures with discrete nonlinearities. Phil. Trans. R. Soc. A, 2015, 373(2051): 20140410.

[5] Lin R M, Ewins D J. Location of localised stiffness non-linearity using measured modal data. Mechanical Systems and Signal Processing, 1995, 9(3): 329-339.

[6] Wang X, Zheng G T. Equivalent Dynamic Stiffness Mapping technique for identifying nonlinear structural elements from frequency response functions. Mechanical Systems and Signal Processing, 2016, 68: 394-415.

[7] Yasuda K, Kawamura S, Watanabe K. Identification of nonlinear multi-degree-of-freedom systems. Presentation of an identification technique. JSME international journal. Ser. 3, Vibration, control engineering, engineering for industry, 1988, 31(1): 8-14.

[8] Al-Hadid M A, Wright J R. Developments in the force-state mapping technique for non-linear systems and the extension to the location of non-linear elements in a lumped-parameter system. Mechanical Systems and Signal

Processing, 1989, 3(3): 269-290.

[9] Benhafsi Y, Penny J E T, Friswell M I. A parametric identification method for discrete nonlinear systems incorporating cubic stiffness elements. International Journal of Analytical and Experimental Modal Analysis, 1992, 7: 179-179.

[10] Liu Y, Shepard W S. Dynamic force identification based on enhanced least squares and total least-squares schemes in the frequency domain. Journal of sound and vibration, 2005, 282(1): 37-60.

[11] Adams R, Doyle J F. Multiple force identification for complex structures. Experimental Mechanics, 2002, 42(1): 25-36.

[12] Wang Z, Lin R M, Lim M K. Structural damage detection using measured FRF data. Computer methods in applied mechanics and engineering, 1997, 147(1): 187-197.

[13] Lin R M. Identification of the dynamic characteristics of nonlinear structures. University of London, 1990.

[14] Siller H R E. Non-linear modal analysis methods for engineering structures. University of London, 2004.

[15] Aykan M, Özgüven H N. Parametric identification of nonlinearity in structural systems using describing function inversion. Mechanical Systems and Signal Processing, 2013, 40(1): 356-376.

[16] Gondhalekar A C. Strategies for Non-Linear System Identification. Imperial College London, 2009.

[17] Shaw A D, Hill T L, Neild S A, et al. Periodic responses of a structure with 3: 1 internal resonance. Mechanical Systems and Signal Processing, 2016, 81:19-34.

[18] Mottershead J E, Link M, Friswell M I. The sensitivity method in finite element model updating: a tutorial. Mechanical systems and signal processing, 2011, 25(7): 2275-2296.

[19] Barton D A W, Mann B P, Burrow S G. Control-based continuation for investigating nonlinear experiments. Journal of Vibration and Control, 2012, 18(4): 509-520.